NANO LETTERS

pubs.acs.org/NanoLett Letter

Induced Superconducting Pairing in Integer Quantum Hall Edge States

Mehdi Hatefipour, Joseph J. Cuozzo, Jesse Kanter, William M. Strickland, Christopher R. Allemang, Tzu-Ming Lu, Enrico Rossi, and Javad Shabani*

Cite This: *Nano Lett.* 2022, 22, 6173−6178 Read Online

ACCESS | Metrics & More | Article Recommendations | Supporting Information

ABSTRACT: Indium arsenide (InAs) near surface quantum wells (QWs) are promising for the fabrication of semiconductor−superconductor heterostructures given that they allow for a strong hybridization between the two-dimensional states in the quantum well and the ones in the superconductor. In this work, we present results for InAs QWs in the quantum Hall regime placed in proximity of superconducting NbTiN. We observe a negative downstream resistance with a corresponding reduction of Hall (upstream) resistance, consistent with a very high Andreev conversion. We analyze the experimental data using the Landauer-Büttiker formalism, generalized to allow for Andreev reflection processes. We attribute the high efficiency of Andreev conversion in our devices to the large transparency of the InAs/NbTiN interface and the consequent strong hybridization of the QH edge modes with the states in the superconductor.

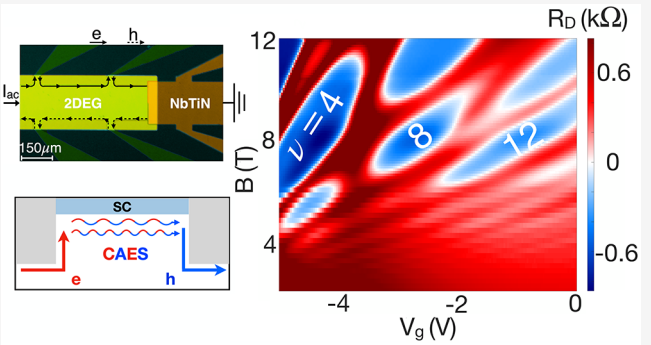

KEYWORDS: *Integer quantum hall effect, Andreev reflection, Superconductivity*

Anyons with non-Abelian statistics are of great fundamental interest[1] and can be used to realize topologically protected, and therefore intrinsically fault-tolerant qubits.[2−4] Non-Abelian anyons are expected to be realized in few fractional quantum Hall (QH) states[5−9] such as the QH states with filling factor $\nu = 5/2$,[10−12] and possibly $\nu = 12/5$.[13] However, so far, no unambiguous experimental confirmation exists of the presence of non-Abelian anyons in such QH states.

An alternative route to realize non-Abelian anyons relies on inducing superconducting pairing between counter-propagating edge modes of QH states that intrinsically support only Abelian anyons.[14−17] These theoretical proposals build on an earlier proposal for creating Majorana zero modes, that is, the anyons with the simplest non-Abelian statistics, using 1D modes at the edge of a 2D topological insulator (TI) in contact with a superconductor (SC).[18] In contrast to TIs, in two-dimensional electron gases (2DEGs) in the QH regime, by varying filling factor ν, states can be realized with a variety of topological orders. This allows access to more exotic edge states needed for engineering anyons with richer non-Abelian statistics. Key in all these theoretical proposals is the ability to induce superconducting pairing, via the proximity effect, between the QH edge modes.

The strength of the superconducting correlations that can be induced in a QH−SC heterojunction can be evaluated by obtaining the amplitude of the Andreev reflection of QH edge modes. The early search for Andreev reflection in QH−SC systems focused on InAs and InGaAs semiconductor magnetoresistance oscillations at relatively low magnetic fields[19] followed later by reports of induced superconductivity in QH states.[20] More recently there have been reports of observation of induced superconductivity,[21,22] cross Andreev reflection,[23,24] edge state mediated supercurrent,[25] and interference of chiral Andreev edge states[26−29] in graphene. To make further progress, it is essential to reliably demonstrate the ability to induce robust superconducting correlations into the edge modes of a QH state.

In this work, we show that in high quality InAs/NbTiN heterostructures, very strong superconducting correlations can be induced in the edge modes of integer QH states realized in the InAs-based quantum wells (QWs). Such correlations appear to be robust, showing no oscillations as a function of doping, for gate voltages within the QH plateaus. We analyze the experimental data in conjunction with a microscopic model to extract the details of the processes determining the transport properties of the QH−SC interface.

Received: April 7, 2022
Revised: July 18, 2022
Published: July 22, 2022

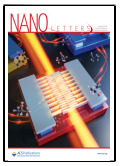

https://doi.org/10.1021/acs.nanolett.2c01413
Nano Lett. 2022, 22, 6173−6178

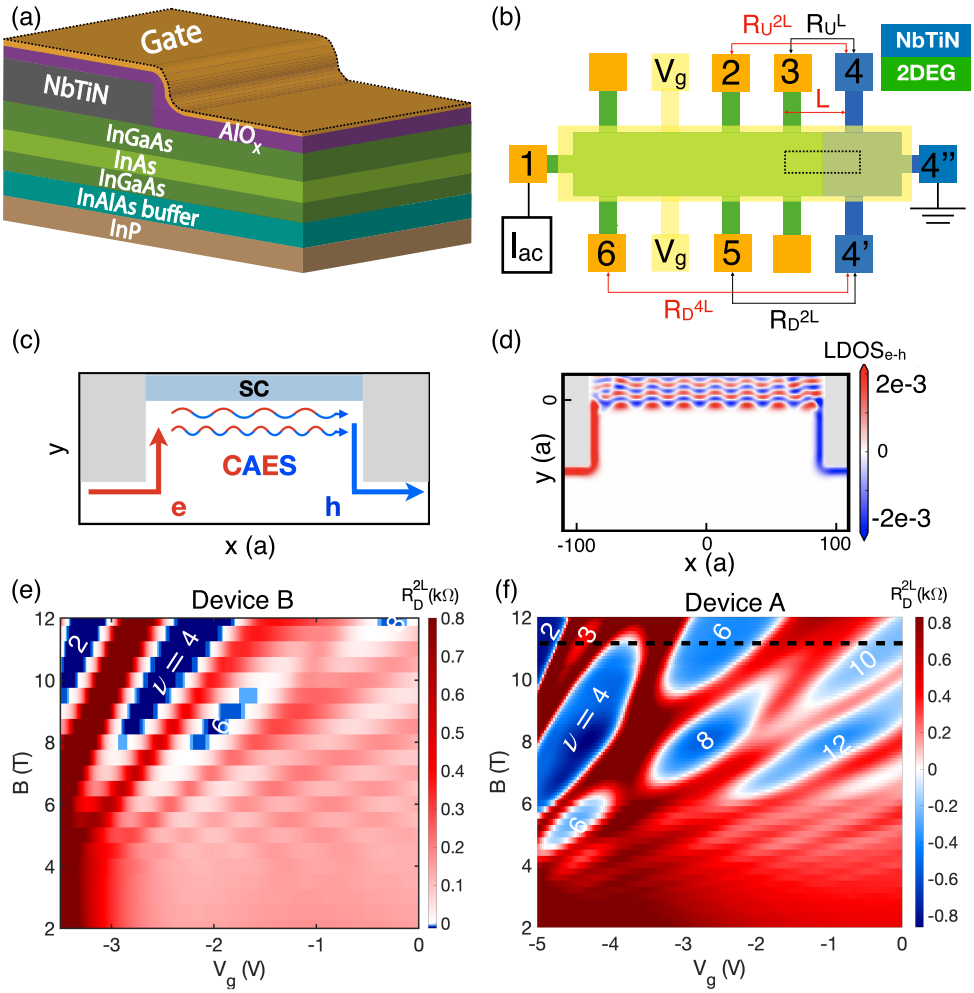

Figure 1. (a) Schematic of gated NbTiN/InAs hybrid device structure (only the portion which is defined by the rectangle in panel b). (b) Device pin−out configuration. Contacts 1, 2, 3, 5, and 6 are normal; contacts 4, 4′, 4″ are superconducting. Contacts 1 and 4″ are used as the source and drain, respectively. Contacts which are not labeled had electrical connection issue during the experiment. (c) Andreev conversion via CAES interference along the QH−SC interface. (d) A supporting tight binding calculation of the difference between the electron and hole LDOS ($LDOS_{e-h}$). (e) Measured R_D^{2L} as a function of V_g and B in a dirty interface device (device B). (f) Measured R_D^{2L} as a function of V_g and B in the cleaned interface device (device A). IQHSs are labeled from complementary R_{xy} data. The dashed line shows the position of the cut shown in Figure 2a.

Figure 1a shows a cross sectional schematic of the fabricated device used in this work. The QW is formed by a 4 nm layer of $In_{0.81}Ga_{0.19}As$ layer, a 7 nm layer of InAs, and a 10 nm top layer of $In_{0.81}Ga_{0.19}As$. The QW is grown on $In_xAl_{1-x}As$ buffer where the indium content is step-graded from $x = 0.52$ to 0.81 to help with dislocations originating from lattice mismatch between InP and quantum well in higher levels. A delta-doped Si layer with electron doping $n \sim 1 \times 10^{12}$ cm^{-2} is placed 6 nm below the QW. This epitaxial structure has been used in previous studies on mesoscopic superconductivity[30−33] in the development of tunable qubits[34] and in studies aimed at realizing and detecting topological superconducting states.[35−37]

A Hall bar, Figure 1b, is fabricated by electron beam lithography. In order to study the 2DEG/SC interface, a 90 nm thick layer of NbTiN was sputtered as the superconducting contacts with a 150 μm-wide interface after performing wet etch surface cleaning (Device A). We also fabricated a similar device with intentional no surface cleaning step before NbTiN sputtering (Device B). A metallic top gate is created by depositing a layer of Al oxide followed by an Al layer to control the QW electron density.[38] The mobility of the QW is determined to be $\mu \sim 12\,000$ cm^2/V·s at $n \sim 8.51 \times 10^{11}$ cm^{-2} corresponding to an electron mean free path of $l_e \sim 180$ nm. All data reported here were taken at $T \sim 30$ mK. We have provided more information on transport properties of the sample in the SI. We note that while we focus mainly on one device (Device A) in the main text, we have studied a few other similar devices which their data have been shown in SI.

When the sample is placed in a magnetic field, in the classical picture electrons and holes will alternate their skipping orbits across the interface of the superconductor and 2DEG.[39] In the full quantum-mechanical analysis the electron and hole edge states hybridize due to the proximity of the SC and form a coherent chiral Andreev edge state (CAES) extended along the QH−SC interface.[27,40,41] A schematic of CAES propagation along the QH−SC interface is shown in Figure 1c. In this picture, if more holes than electrons reach the normal lead downstream from the superconducting electrode (lead 5), then a negative potential difference ($V_5 - V_4'$) develops. In Figure 1d, we show the local density of states (LDOS) of a CAES obtained with a tight binding (TB) calculation performed using the python package Kwant.[42] In the TB model, the

https://doi.org/10.1021/acs.nanolett.2c01413
Nano Lett. 2022, 22, 6173−6178

presence of the magnetic field is taken into account via a Peierls phase, and the superconductivity of the QW proximitized by NbTiN via a mean field an s-wave pairing term of strength $\tilde{\Delta}$. The details of the TB model can be found in the SI.

Figure 1e,f shows the results for the downstream resistance, R_D^{2L}, measured between the voltage contacts 5 and 4′, as a function of gate voltage V_g and magnetic field B. Hall resistance data measured between contacts 2 and 5 allow us to determine the filling factor of the different regions of Figure 1e,f. Figure 2a shows the horizontal cut at B = 11 T of Figure 1f, R_D^{4L}, and

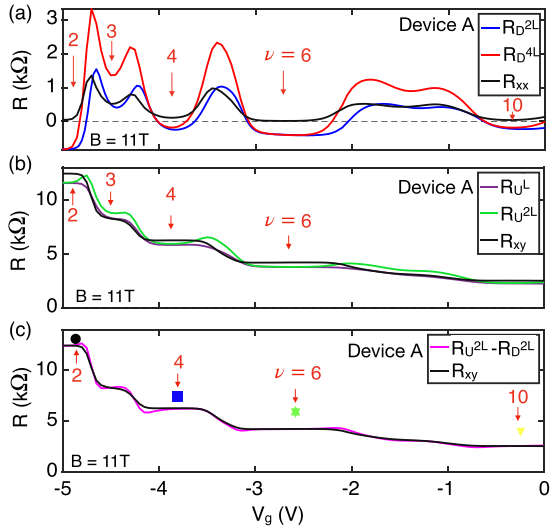

Figure 2. (a) R_D^{2L}, R_D^{4L}, and R_{xx} (Device A), (b) R_U^{L}, and R_{xy} (Device A), (c) $R_U - R_D$ and R_{xy} shown as a function of V_g. All traces taken at B = 11 T (Device A). IQHSs are labeled and markers are shown for the states used in Figure 3c.

the corresponding longitudinal resistance R_{xx}. From the R_{xx} measurements, we see that we have well developed integer QH states (IQHS). From Figures 1f and 2a, we clearly observe that R_D is negative for IQHS, a fact that strongly suggests the presence of Andreev processes at the QH−SC interface for these IQHS. The similarity of R_D^{2L} and R_D^{4L} also is a hint of IQHS being dissipationless states; therefore, going farther from the interface does not affect the magnitude of the negative resistance value. We notice the importance of a clean InAs/NbTiN interface by comparing the magnitude of negative resistance in Figure 1e,f. The clean interface on device A has been achieved by etching the surface of defined NbTiN pattern area by buffered oxide etchant (BOE) for 2 s immediately followed by loading into sputtering tool's chamber in order to minimize the time for the native oxide growth at the interface. On the other hand, for device B this cleaning step has been skipped and NbTiN sputtered on the defined region after its exposure to air. For the rest of the paper, we focus only on device A results. The upstream resistance R_U^{2L} (measured between contacts 3 and 4) exhibits plateaus corresponding to the R_{xy} plateaus in the magnetic field but with resistance values lower than R_{xy} (Figure 2b). Moreover, $R_U^{2L} - R_D^{2L}$ recovers the quantized Hall value, R_{xy}, as shown in Figure 2c. Note that this difference does not necessarily match the R_{xy} data outside the QH regime.

These results can be understood within the Landauer-Büttiker (LB) theory, generalized to allow for the presence of a superconducting lead.[43,44]

We start with the six-terminal setup shown in Figure 1b (see also the SI). We assume the terminal 1, 2, 3, 5, 6 to be ideal metallic leads, and contact 4 to be a superconducting lead. We first consider the limit in which no normal reflection or transmission processes take place at the superconducting lead. I_i and V_i, the currents and voltages, respectively, are allowed at the terminals i = (1, 2, 3, 4, 5, 6). Without loss of generality, we can set V_4 = 0. We can use the charge conservation equation $\sum_i I_i = 0$ to express I_4 in terms of the currents at the other leads. With these considerations, the LB equations reduce to the following system of linear equations

$$\begin{pmatrix} I_1 \\ I_2 \\ I_3 \\ I_5 \\ I_6 \end{pmatrix} = \frac{\nu}{R_H} \begin{pmatrix} 1 & 0 & 0 & 0 & -1 \\ -1 & 1 & 0 & 0 & 0 \\ 0 & -1 & 1 & 0 & 0 \\ 0 & 0 & 2A-1 & 1 & 0 \\ 0 & 0 & 0 & -1 & 1 \end{pmatrix} \begin{pmatrix} V_1 \\ V_2 \\ V_3 \\ V_5 \\ V_6 \end{pmatrix} \quad (1)$$

where ν is the number of edge states, R_H is the Hall resistance, and A is the average probability, per edge mode, of Andreev reflection. Considering that no current flows into leads 2, 3, 5, 6, so that $I_2 = I_3 = I_5 = I_6 = 0$, $V_1 = V_2 = V_3$, $V_5 = V_6$, and setting $I \equiv I_1$, it is straightforward to solve eq 1 to obtain

$$R_U^{2L} = \frac{V_2}{I} = \frac{R_H}{\nu}\frac{1}{2A} \quad (2)$$

$$R_D^{2L} = \frac{V_5}{I} = \frac{R_H}{\nu}\left(\frac{1}{2A} - 1\right) \quad (3)$$

Figure 3a shows the scaling of R_D with respect to $1/\nu$ for different values of B. From the slope of the fits to the experimental data shown in Figure 3a, we obtain the value of A_{exp} = 55%, independent, to very good approximation, on the value of V_g within the QH plateaus (Figure 3b). It is instructive to compare our work with two other classes of experiments. First, studies based on graphene-MoRe, see ref 26, where the value of R_D oscillates significantly with B and gate voltage, and therefore there is no well-defined value of A. Second, studies based on graphene-NbTiN, see ref 23, in which a narrow and long superconducting electrode is placed perpendicular to the vacuum edge of the QH system. This geometry allows for additional processes, cross-Andreev-reflection (CAR) processes that are not present in our setup and the setup in ref 26. From the value of R_D at ν = 1 in ref 23, we extract a value of A_{exp} = 50.5% but the comparison to our setup is not straightforward due to the presence of CAR processes. We emphasize that in addition to the large value of A, a unique feature of our devices is the lack of oscillations as a function of V_g and B despite a QH−SC interface that is more than an order of magnitude longer than in the experiments in refs 23 and 26, and that this suggests that in QH−SC based on InAs/SC the CAES might have an extremely long coherence length.

Figure 3c shows the consistency of the measured values of R_D^{2L} and R_U^{2L} with the LB predictions by plotting the ratio $(R_U^{2L} - R_U^{2L})/R_{xy}$ as a function of B that, according to eqs 2 and 3, is expected to be equal to 1.

To understand qualitatively how such values of A can arise, we consider an effective 1D Bogoliubov de Gennes

https://doi.org/10.1021/acs.nanolett.2c01413
Nano Lett. 2022, 22, 6173−6178

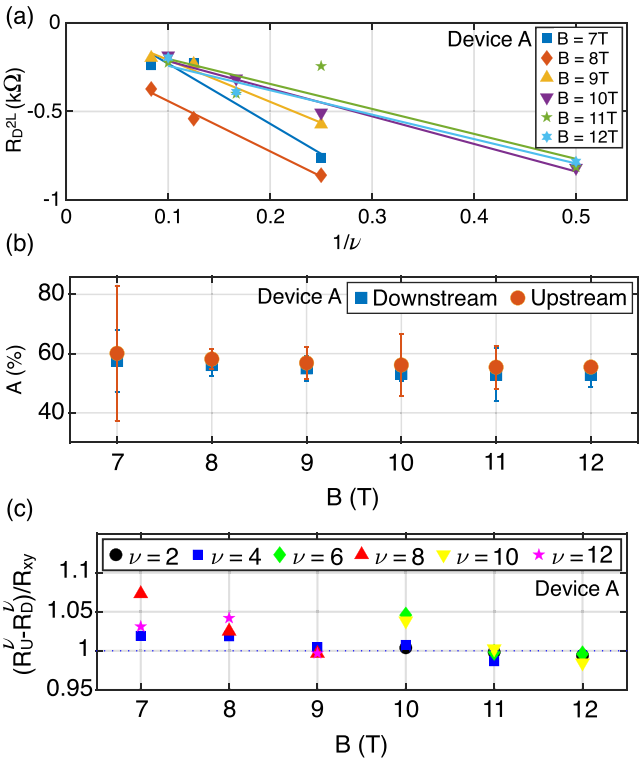

Figure 3. (a) R_D^{2L} versus $1/\nu$ for different IQHSs and values of B, and linear fits corresponding to each magnetic field. (b) A obtained from the slope of linear fits to R_D and R_U data versus $1/\nu$ with their corresponding error bars. (c) $(R_U^{2L} - R_D^{2L})/R_{xy}^\nu$ for different νversus and values of B.

Hamiltonian, H_{BdG}, for the 1D chiral edge modes: $H_{BdG} = \int dx \psi^\dagger(x)\mathcal{H}(x)\psi(x)$ where $\psi(x) = (c_{x\uparrow}, c_{x\downarrow}^\dagger)$ is the spinor formed by the annihilation (creation) operator $c_{x\uparrow}$, $(c_{x\downarrow}^\dagger)$ for a Fermion at position x and spin up (down) and $\mathcal{H}(x) = v_d(-i\partial_x)\tau_0 - v_d k_F \tau_z + \tilde{\Delta}\tau_x$. Here and in the remainder of this Letter, we set $\hbar = 1$. In the equation for $H(x)$, v_d is the drift velocity of the edge modes, τ_i values are the Pauli matrices in Nambu space, k_F is the edge modes Fermi wave vector number (measured with respect to the QH−SC interface), and $\tilde{\Delta}$ is the superconducting superconductor pairing induced via the proximity effect by of the superconducting lead. Using the expression for H, we can obtain the transfer matrix M relating $\psi(x)$ at the two ends of the length L_{sc} of the QH−SC interface of length L_{sc} (see SI),[40,45] and then the expression for the electron−hole conversion probability will be

$$A = \frac{\sin^2(\delta\phi)}{[1 + (v_d k_F/\tilde{\Delta})^2]} \tag{4}$$

In eq 4, $\delta\phi$ is the difference of the phases accumulated by the electron-like and hole-like edge modes along the length of the QH−SC interface. Let $k_F^{(e)}$, $k_F^{(h)}$ be the Fermi wave vector of the electron-like and hole-like edge modes, and $\delta k \equiv |k_F^{(e)} - k_F^{(h)}| = [\tilde{\Delta}^2 + (v_d k_F)^2]^{1/2}/v_d$. We then write $\delta\phi = L_{sc}\delta k$.

Considering that $L_{sc} = 150$ μm is quite large, any small change of δk induced, for example, by changes in V_g should result in a significant change of A and therefore of R_U and R_D. However, in the experiment within the QH plateaus, R_U and R_D do not show any oscillation as a function of V_g. It is natural to conclude that this might be due to scattering processes leading to a dephasing of the electron-like and hole-like modes along the QH−SC interface.[28] In this case, the effective A_{eff} can be obtained by averaging over L_{sc} on the right-hand side of eq 4 to obtain $A_{eff} = \langle A \rangle = 1/(2[1 + (v_d k_F/\tilde{\Delta})^2])$. Considering that $(v_d k_F/\tilde{\Delta})^2 > 0$, we see that in this case we cannot recover the value of A extracted from the experimental results, $A = 0.55 > 0.5$.

To explain the large value of A, accompanied by the lack of oscillations as a function of V_g, we are led to two possibilities. The first possibility is that δ_k does not change appreciably as a function of V_g. From eq 4, considering that $0 < \sin^2(\delta\phi) < 1$, we can see that to have $A = 0.55$ we must have $v_d k_F/\tilde{\Delta} < 0.9$. In the limit when $\delta\phi$ is such that $\sin^2(\delta\phi) \approx 0.55$, we must have $v_d k_F/\tilde{\Delta} \ll 1$. In this limit we can write $\delta k \approx \tilde{\Delta}/v_d$. In good approximation, $\tilde{\Delta}$ and v_d are independent of V_g, and we recover the observed values of R_U and R_D with no oscillations in the QH plateaus. Notice that the condition $v_d k_F/\tilde{\Delta} \ll 1$ is equivalent to the condition $\delta k \xi \approx 1$, where $\xi \equiv v_d/\Delta$ can be interpreted as the superconducting coherence length of the edge modes in proximity of the SC. The other possibility is that dephasing processes are accompanied by a finite probability of single electron tunneling into the superconductor and breaking of particle-hole (p-h) symmetry. This would allow to have a situation in which electron-like states are more likely than h-like states to tunnel into the superconductor and therefore contribute less to the downstream current explaining a negative R_D even when $A \leq 1/2$. If we denote by T the probability, per edge mode, of an electron-like state to tunnel in the SC, in eqs 2 and 3 we would replace $2A$ with $2A + T$. In this case, from the measurements of R_U and R_D we recover $2A + T$. Assuming $\langle A \rangle = 1/2$ would imply $T = 0.2$. The smallest value of $\langle A \rangle$, consistent with particle conservation, is 15% to which it would correspond $T = 0.8$, a value that implies a very strong breaking of particle-hole symmetry at the QH−SC interface. It is difficult to distinguish between these two possibilities given that we cannot measure separately the quasiparticle and supercurrent contributions to the charge current flowing from the QH region into the superconducting lead.

In conclusion, we have fabricated a quantum Hall-superconductor (QH−SC) epitaxial heterostructure based on InAs and NbTiN and characterized the transport properties of its QH edge modes propagating along a superconducting interface. We have observed negative values for the downstream resistance R_D between a normal lead and the superconducting lead and a corresponding suppression of the upstream resistance R_U such that in the QH plateaus the difference $R_U - R_D$ is equal to the Hall resistance R_H. The negative values of R_D are an unambiguous sign that at the QH−SC interface there is a very large electron−hole conversion probability, A. Using a Landauer-Büttiker analysis, we were able to explain the relation between R_D and R_U and express both resistances in terms of a single effective probability for Andreev reflections at the QH−SC interface. Our analysis led us to the conclusion that either the edge modes propagate along the QH−SC interface with negligible dephasing resulting in an electron−hole conversion close to 55%, or if dephasing processes dominate that a strong breaking of particle-hole symmetry at the QH−SC interface must occur. The interface could be further improved by hybrid methods of epitaxial superconductors and semiconductors.[46]

Even the lower bounds' estimates for A that we extract from our measurements are remarkable, larger than any published

https://doi.org/10.1021/acs.nanolett.2c01413
Nano Lett. 2022, 22, 6173−6178

results for QH−SC devices. This shows that in our InAs devices very strong superconducting correlations can be induced into the QH edge modes, an essential prerequisite to use QH−SC heterojunctions to realize non-Abelian anyons and topologically protected qubits and quantum gates based on such unusual quantum states.

■ ASSOCIATED CONTENT

Supporting Information

The Supporting Information is available free of charge at https://pubs.acs.org/doi/10.1021/acs.nanolett.2c01413.

2DEG characterization of device A, nanofabrication details, data for other fabricated devices for this study, Landauer-Büttiker edge state model, derivation of Andreev reflection probability A, effect of electron tunneling into the superconductor, and tight binding model details (PDF)

■ AUTHOR INFORMATION

Corresponding Author

Javad Shabani − *Center for Quantum Phenomena, Department of Physics, New York University, New York, New York 10003, United States;* orcid.org/0000-0002-0812-2809; Email: jshabani@nyu.edu

Authors

Mehdi Hatefipour − *Center for Quantum Phenomena, Department of Physics, New York University, New York, New York 10003, United States*

Joseph J. Cuozzo − *Department of Physics, William & Mary, Williamsburg, Virginia 23187, United States*

Jesse Kanter − *Center for Quantum Phenomena, Department of Physics, New York University, New York, New York 10003, United States*

William M. Strickland − *Center for Quantum Phenomena, Department of Physics, New York University, New York, New York 10003, United States*

Christopher R. Allemang − *Sandia National Laboratories, Albuquerque, New Mexico 87185, United States*

Tzu-Ming Lu − *Sandia National Laboratories, Albuquerque, New Mexico 87185, United States; Center for Integrated Nanotechnologies, Sandia National Laboratories, Albuquerque, New Mexico 87123, United States;* orcid.org/0000-0002-3363-1226

Enrico Rossi − *Department of Physics, William & Mary, Williamsburg, Virginia 23187, United States*

Complete contact information is available at: https://pubs.acs.org/10.1021/acs.nanolett.2c01413

Notes

The authors declare no competing financial interest.

■ ACKNOWLEDGMENTS

We thank Dr. Shashank Misra for his insightful comment and feedback. The NYU team acknowledge partial support from DARPA Grant DP18AP900007 and ONR Grant N00014-21-1-2450. J.J.C. and E.R. acknowledge support from ARO Grant W911NF-18-1-0290. E.R. acknowledges the Aspen Center for Physics, which is supported by National Science Foundation grant PHY-1607611. J.J.C. also acknowledges support from the Graduate Research Fellowship awarded by the Virginia Space Grant Consortium (VSGC). Sandia National Laboratories is a multimission laboratory managed and operated by National Technology and Engineering Solutions of Sandia LLC, a wholly owned subsidiary of Honeywell International Inc. for the U.S. DOE's National Nuclear Security Administration under contract DE-NA0003525. This work was performed, in part, at the Center for Integrated Nanotechnologies, a U.S. DOE, Office of BESs, user facility. This paper describes objective technical results and analysis. Any subjective views or opinions that might be expressed in the paper do not necessarily represent the views of the U.S. DOE or the United States Government.

■ REFERENCES

(1) Moore, G.; Read, N. Nonabelions in the fractional quantum hall effect. *Nuclear Physics B* **1991**, *360*, 362−396.

(2) Kitaev, A. Fault-tolerant quantum computation by anyons. *Annals of Physics* **2003**, *303*, 2−30.

(3) Das Sarma, S.; Freedman, M.; Nayak, C. Topologically Protected Qubits from a Possible Non-Abelian Fractional Quantum Hall State. *Phys. Rev. Lett.* **2005**, *94*, 166802.

(4) Nayak, C.; Simon, S. H.; Stern, A.; Freedman, M.; Das Sarma, S. Non-Abelian anyons and topological quantum computation. *Rev. Mod. Phys.* **2008**, *80*, 1083−1159.

(5) Read, N.; Green, D. Paired states of fermions in two dimensions with breaking of parity and time-reversal symmetries and the fractional quantum Hall effect. *Phys. Rev. B* **2000**, *61*, 10267−10297.

(6) Cheng, M. Superconducting proximity effect on the edge of fractional topological insulators. *Phys. Rev. B* **2012**, *86*, 195126.

(7) Alicea, J.; Fendley, P. Topological Phases with Parafermions: Theory and Blueprints. *Annual Review of Condensed Matter Physics* **2016**, *7*, 119−139.

(8) Vaezi, A. Fractional topological superconductor with fractionalized Majorana fermions. *Phys. Rev. B* **2013**, *87*, 035132.

(9) Vaezi, A. Superconducting Analogue of the Parafermion Fractional Quantum Hall States. *Phys. Rev. X* **2014**, *4*, 031009.

(10) Willett, R.; Eisenstein, J. P.; Störmer, H. L.; Tsui, D. C.; Gossard, A. C.; English, J. H. Observation of an even-denominator quantum number in the fractional quantum Hall effect. *Phys. Rev. Lett.* **1987**, *59*, 1776−1779.

(11) Miller, J. B.; Radu, I. P.; Zumbühl, D. M.; Levenson-Falk, E. M.; Kastner, M. A.; Marcus, C. M.; Pfeiffer, L. N.; West, K. W. Fractional quantum Hall effect in a quantum point contact at filling fraction 5/2. *Nat. Phys.* **2007**, *3*, 561−565.

(12) Radu, I. P.; Miller, J. B.; Marcus, C. M.; Kastner, M. A.; Pfeiffer, L. N.; West, K. W. Quasi-Particle Properties from Tunneling in the v = 5/2 Fractional Quantum Hall State. *Science* **2008**, *320*, 899−902.

(13) Zhu, W.; Gong, S. S.; Haldane, F. D. M.; Sheng, D. N. Fractional Quantum Hall States at ν = 13/5 and 12/5 and Their Non-Abelian Nature. *Phys. Rev. Lett.* **2015**, *115*, 126805.

(14) Qi, X.-L.; Hughes, T. L.; Zhang, S.-C. Chiral topological superconductor from the quantum Hall state. *Phys. Rev. B* **2010**, *82*, 184516.

(15) Lindner, N. H.; Berg, E.; Refael, G.; Stern, A. Fractionalizing Majorana Fermions: Non-Abelian Statistics on the Edges of Abelian Quantum Hall States. *Phys. Rev. X* **2012**, *2*, 041002.

(16) Clarke, D. J.; Alicea, J.; Shtengel, K. Exotic circuit elements from zero-modes in hybrid superconductor−quantum-Hall systems. *Nat. Phys.* **2014**, *10*, 877−882.

(17) Mong, R. S. K.; Clarke, D. J.; Alicea, J.; Lindner, N. H.; Fendley, P.; Nayak, C.; Oreg, Y.; Stern, A.; Berg, E.; Shtengel, K.; Fisher, M. P. A. Universal Topological Quantum Computation from a Superconductor-Abelian Quantum Hall Heterostructure. *Phys. Rev. X* **2014**, *4*, 011036.

(18) Fu, L.; Kane, C. L. Superconducting Proximity Effect and Majorana Fermions at the Surface of a Topological Insulator. *Phys. Rev. Lett.* **2008**, *100*, 096407.

(19) Nitta, J.; Akazaki, T.; Takayanagi, H. Magnetic-field dependence of Andreev reflection in a clean Nb-InAs-Nb junction. *Physical review. B, Condensed matter* **1994**, *49*, 3659−3662.
(20) Wan, Z.; Kazakov, A.; Manfra, M. J.; Pfeiffer, L. N.; West, K. W.; Rokhinson, L. P. Induced superconductivity in high-mobility two-dimensional electron gas in gallium arsenide heterostructures. *Nat. Commun.* **2015**, *6*, 7426.
(21) Rickhaus, P.; Weiss, M.; Marot, L.; Schönenberger, C. Quantum Hall Effect in Graphene with Superconducting Electrodes. *Nano Lett.* **2012**, *12*, 1942.
(22) Park, G.-H.; Kim, M.; Watanabe, K.; Taniguchi, T.; Lee, H.-J. Propagation of superconducting coherence via chiral quantum-Hall edge channels. *Sci. Rep.* **2017**, *7*, 10953.
(23) Gül, O.; Ronen, Y.; Lee, S. Y.; Shapourian, H.; Zauberman, J.; Lee, Y. H.; Watanabe, K.; Taniguchi, T.; Vishwanath, A.; Yacoby, A.; Kim, P. Andreev Reflection in the Fractional Quantum Hall State. *Phys. Rev. X* **2022**, *12*, 021057.
(24) Lee, G.-H.; Huang, K.-F.; Efetov, D. K.; Wei, D. S.; Hart, S.; Taniguchi, T.; Watanabe, K.; Yacoby, A.; Kim, P. Inducing superconducting correlation in quantum Hall edge states. *Nat. Phys.* **2017**, *13*, 693−698.
(25) Amet, F.; Ke, C. T.; Borzenets, I. V.; Wang, J.; Watanabe, K.; Taniguchi, T.; Deacon, R. S.; Yamamoto, M.; Bomze, Y.; Tarucha, S.; Finkelstein, G. Supercurrent in the quantum Hall regime. *Science* **2016**, *352*, 966−969.
(26) Zhao, L.; Arnault, E. G.; Bondarev, A.; Seredinski, A.; Larson, T. F. Q.; Draelos, A. W.; Li, H.; Watanabe, K.; Taniguchi, T.; Amet, F.; Baranger, H. U.; Finkelstein, G. Interference of chiral Andreev edge states. *Nat. Phys.* **2020**, *16*, 862−867.
(27) Hoppe, H.; Zülicke, U.; Schön, G. Andreev Reflection in Strong Magnetic Fields. *Phys. Rev. Lett.* **2000**, *84*, 1804−1807.
(28) Kurilovich, V. D.; Raines, Z. M.; Glazman, L. I. Disorder in Andreev reflection of a quantum Hall edge. *arXiv*, 2022, 2201.00273 (accessed Jan. 2, 2022) https://arxiv.org/abs/2201.00273.
(29) Manesco, A. L. R.; Flór, I. M.; Liu, C.-X.; Akhmerov, A. R. Mechanisms of Andreev reflection in quantum Hall graphene. *arXiv*, 2021, 2103.06722 (accessed Feb. 15, 2022) https://arxiv.org/abs/2103.06722.
(30) Kjaergaard, M.; Nichele, F.; Suominen, H.; Nowak, M.; Wimmer, M.; Akhmerov, A.; Folk, J.; Flensberg, K.; Shabani, J.; Palmstrøm, C.; Marcus, C. Quantized conductance doubling and hard gap in a two-dimensional semiconductor-superconductor heterostructure. *Nat. Commun.* **2016**, *7*, 12841.
(31) Bøttcher, C. G. L.; Nichele, F.; Kjaergaard, M.; Suominen, H. J.; Shabani, J.; Palmstrøm, C. J.; Marcus, C. M. Superconducting, insulating and anomalous metallic regimes in a gated two-dimensional semiconductor-superconductor array. *Nat. Phys.* **2018**, *14*, 1138−1144.
(32) Mayer, W.; Yuan, J.; Wickramasinghe, K. S.; Nguyen, T.; Dartiailh, M. C.; Shabani, J. Superconducting proximity effect in epitaxial Al-InAs heterostructures. *Appl. Phys. Lett.* **2019**, *114*, 103104.
(33) Mayer, W.; Dartiailh, M. C.; Yuan, J.; Wickramasinghe, K. S.; Rossi, E.; Shabani, J. Gate controlled anomalous phase shift in Al/InAs Josephson junctions. *Nat. Commun.* **2020**, *11*, 212.
(34) Casparis, L.; Pearson, N. J.; Kringhøj, A.; Larsen, T. W.; Kuemmeth, F.; Nygård, J.; Krogstrup, P.; Petersson, K. D.; Marcus, C. M. Voltage-controlled superconducting quantum bus. *Phys. Rev. B* **2019**, *99*, 085434.
(35) Suominen, H. J.; Kjaergaard, M.; Hamilton, A. R.; Shabani, J.; Palmstrøm, C. J.; Marcus, C. M.; Nichele, F. Zero-Energy Modes from Coalescing Andreev States in a Two-Dimensional Semiconductor-Superconductor Hybrid Platform. *Phys. Rev. Lett.* **2017**, *119*, 176805.
(36) Fornieri, A.; et al. Evidence of topological superconductivity in planar Josephson junctions. *Nature* **2019**, *569*, 89−92.
(37) Dartiailh, M. C.; Cuozzo, J. J.; Elfeky, B. H.; Mayer, W.; Yuan, J.; Wickramasinghe, K. S.; Rossi, E.; Shabani, J. Missing Shapiro steps in topologically trivial Josephson junction on InAs quantum well. *Nat. Commun.* **2021**, *12*, 78.
(38) Shabani, J.; Kjaergaard, M.; Suominen, H. J.; Kim, Y.; Nichele, F.; Pakrouski, K.; Stankevic, T.; Lutchyn, R. M.; Krogstrup, P.; Feidenhans'l, R.; Kraemer, S.; Nayak, C.; Troyer, M.; Marcus, C. M.; Palmstrøm, C. J. Two-dimensional epitaxial superconductor-semiconductor heterostructures: A platform for topological superconducting networks. *Phys. Rev. B* **2016**, *93*, 155402.
(39) Chtchelkatchev, N. M.; Burmistrov, I. S. Conductance oscillations with magnetic field of a two-dimensional electron gas-superconductor junction. *Phys. Rev. B* **2007**, *75*, 214510.
(40) van Ostaay, J. A. M.; Akhmerov, A. R.; Beenakker, C. W. J. Spin-triplet supercurrent carried by quantum Hall edge states through a Josephson junction. *Phys. Rev. B* **2011**, *83*, 195441.
(41) Khaymovich, I. M.; Chtchelkatchev, N. M.; Shereshevskii, I. A.; Mel'nikov, A. S. Andreev transport in two-dimensional normal-superconducting systems in strong magnetic fields. *EPL (Europhysics Letters)* **2010**, *91*, 17005.
(42) Groth, C. W.; Wimmer, M.; Akhmerov, A. R.; Waintal, X. Kwant: a software package for quantum transport. *New J. Phys.* **2014**, *16*, 063065.
(43) Datta, S.; Bagwell, P. F.; Anantram, M. P. *Scattering Theory of Transport for Mesoscopic Superconductors*, ECE Technical Reports, Paper 107; Purdue University, **1996**.
(44) Beconcini, M.; Polini, M.; Taddei, F. Nonlocal superconducting correlations in graphene in the quantum Hall regime. *Phys. Rev. B* **2018**, *97*, 201403.
(45) Gao, H.; Xue, H.; Wang, Q.; Gu, Z.; Liu, T.; Zhu, J.; Zhang, B. Observation of topological edge states induced solely by non-Hermiticity in an acoustic crystal. *Phys. Rev. B* **2020**, *101*, 180303.
(46) Drachmann, A. C. C.; Suominen, H. J.; Kjaergaard, M.; Shojaei, B.; Palmstrøm, C. J.; Marcus, C. M.; Nichele, F. Proximity Effect Transfer from NbTi into a Semiconductor Heterostructure via Epitaxial Aluminum. *Nano Lett.* **2017**, *17*, 1200−1203.

https://doi.org/10.1021/acs.nanolett.2c01413
Nano Lett. 2022, 22, 6173−6178

Supplementary Information: Induced superconducting pairing in integer quantum Hall edge states

Mehdi Hatefipour[1], Joseph J. Cuozzo[2], Jesse Kanter[1], William M. Strickland[1], Christopher R. Allemang[3], Tzu-Ming Lu[3,4], Enrico Rossi[2], and Javad Shabani[1*]

[1] *Center for Quantum Phenomena, Department of Physics, New York University, NY 10003, USA*

[2] *Department of Physics, William & Mary, Williamsburg, Virginia 23187, USA*

[3] *Sandia National Laboratories, Albuquerque, New Mexico 87185, USA*

[4] *Center for Integrated Nanotechnologies, Sandia National Laboratories, Albuquerque, New Mexico, 87123, USA*

(Dated: July 12, 2022)

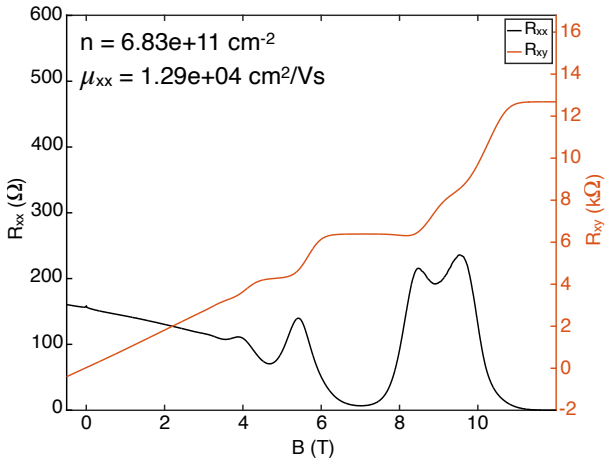

FIG. 1. Magnetotransport data using Van der Pauw method on a $5mm \times 5mm$ piece of wafer used in this paper prior to the fabrication taken at $T = 1.5K$ in a 12-tesla teslatron system.

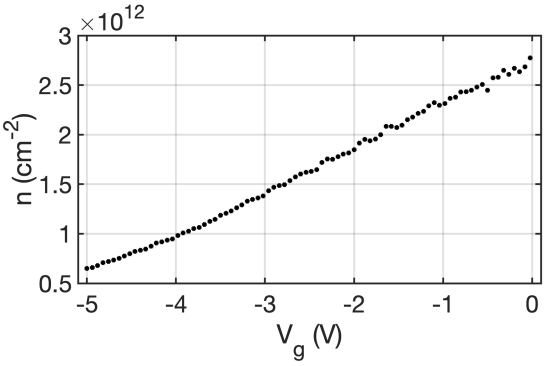

FIG. 2. Carrier density calculated from the fit to the linear regime of hall resistance vs applied gate voltage to the device.

I. EXPERIMENT

Figure 1 shows the 2DEG characterization data of the wafer used in this paper before fabrication. The experiment setup is a 4-point measurement using Van der Pauw method performed in a Teslatron system (Oxford instrument) with a maximum perpendicular magnetic field of 12 T and base temperature of 1.5 K. The sheet density and mobility reported on the plot are calculated from the slope of linear region of Hall resistance and longitudinal

* jshabani@nyu.edu

resistance of the sample at zero magnetic field respectively.

In device A, we have measured the density corresponding to each gate voltage from the Hall measurement. Figure 2 shows the mapping from applied gate voltage to the density of carriers. The density (n) is calculated based the linear regime of Hall resistance. Figure 3 shows the corresponding mobility of the Hall-bar in Fig. 2 is calculated based on the longitudinal resistance in 2DEG at zero magnetic field, density and geometric factor of the Hall-bar.

Figure 5 shows a falsed-colored optical image of the real device used in the experiment. Arrows in the photo show the edge modes going around the 2DEG and being reflected as holes in the ideal scenario from the superconducting contact as a result of Andreev electron-hole conversion.

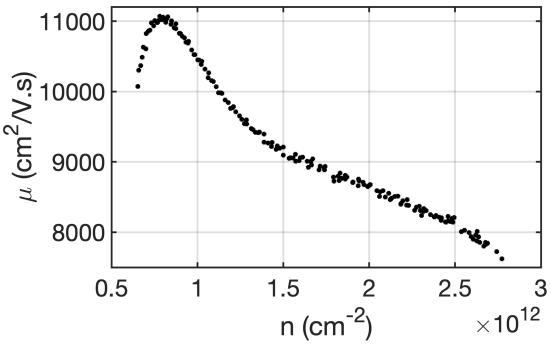

FIG. 3. Mobility of carries calculated from longitudinal resistance vs carrier density.

We characterized the sputtered NbTiN part of the device independently by 3-point measurement setup using only the superconducting contacts. The resulting film has a critical magnetic field at zero temperature of $B_c = 28$T and critical temperature of $T_c = 13.6$K

Figure 7 shows the scaling of R_U with respect to $1/\nu$ for different values of B. This is the complementary data to Fig. 3 (a) in the main text. The A parameter in Fig. 3 (b) in the main text for upstream data has been calculated based on the slope of lines in Fig. 7.

FABRICATION DETAILS

Table I provides the fabrication details on different devices used in this experiment.

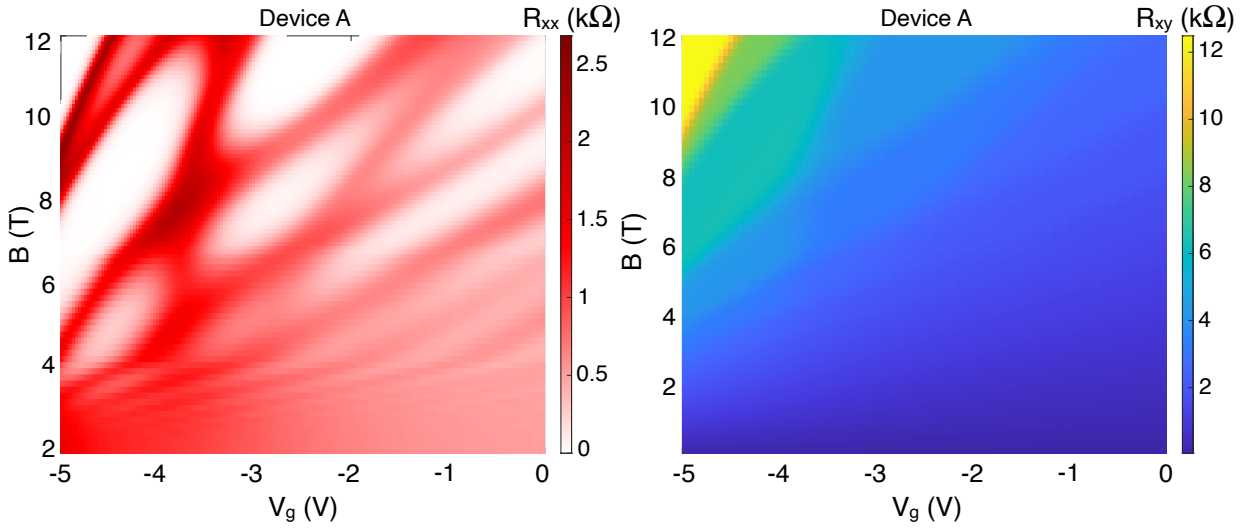

FIG. 4. R_{xx} and R_{xy} from device A for different top gate voltages and magnetic field.

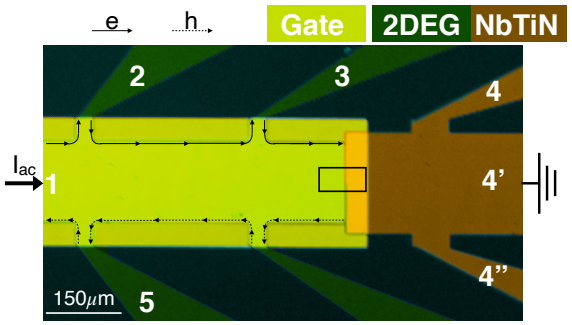

FIG. 5. Falsed-colored optical image of the real device shows various pads for both 2DEG and NbTiN allowing us to characterize each individually. We can also see the contacts used to source and drain the AC current from lock-in amplifier for 4-pt measurement setup as well as the top gate indicated by yellow color.

Figure 8 shows the negative downstream signal has been observed in multiple samples. Observation of this phenomena is highly sensitive to the fabrication process. In the main text, we mainly discuss the results of the device A which has the strongest signal among all the devices we fabricated for this experiment. In all devices, we have also measured R_D on the other edge by flipping the magnetic field sign and typically observe a different negative value. One possible explanation could be for different chiralities the paths of the edge modes

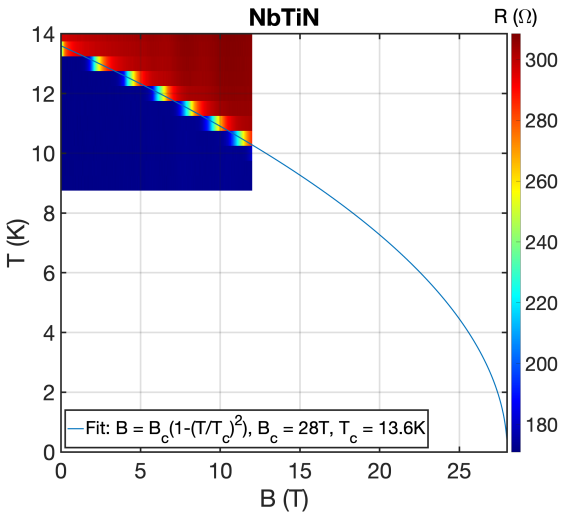

FIG. 6. characterizing the sputtered NbTiN on device using only superconducting contacts by taking magnetic field sweeps at different fixed temperatures from 8K to 14K with 0.5K intervals.

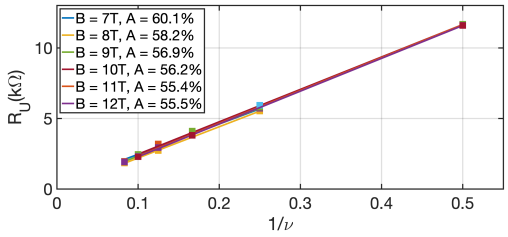

FIG. 7. R_U vs $1/\nu$ for different IQHSs and values of B, and linear fits corresponding to each magnetic field (Device A).

are different.

II. THEORY

A. Landauer-Büttiker edge state model

Figure 9 shows schematically the setup that we considered in the main text to obtain the Landauer-Büttiker equations. Let V_i, I_i, with $i = 1, 2, 3, 4, 5, 6$, be the voltages and currents, respectively, at the 6 different leads shown by the yellow and blue pads in Fig. 9. Let ν be the QH filling factor. We assume the lead 4 to be superconducting. We first restrict ourselves to

Device	Lithography method	2DEG/SC length	Surface cleaning prior to sputtering	Fabrication location
A	E-beam	150 μm	2s BOE etch	Sandia Lab
B	E-beam	100 μm	no cleaning	NYU
C	E-beam	25 μm	no cleaning	NYU
D	Photo	50 μm	no cleaning	NYU
E	Photo	150 μm	2s BOE etch	Sandia Lab

TABLE I. Fabrication details of the various devices labeled by A to E used in this experiment. The major differences in the fabrication of these devices which each of them could potentially play an important role in the quality of the device is highlighted in this table.

the case when only Andreev reflection processes, with probability A, can take place at the superconducting lead, so that all the charge current flowing out of lead 4 is a supercurrent. All the other leads are assumed to be ideal metallic leads. Without loss of generality, we can set $V_4 = 0$. Charge current I is injected in lead 1 and drained at lead 4, all the other contacts are assumed to be floating, so that $I_1 = I$, $I_4 = -I$, $I_2 = I_3 = I_5 = I_6 = 0$. Given their chiral nature, QH edge modes cannot backscatter so that the transmission probability between consecutive metallic leads can be taken to be equal to 1. In these conditions the Landauer-Büttiker equations for the edge modes take the form:

$$\begin{pmatrix} I_1 \\ I_2 \\ I_3 \\ I_5 \\ I_6 \end{pmatrix} = \frac{\nu}{R_H} \begin{pmatrix} 1 & 0 & 0 & 0 & -1 \\ -1 & 1 & 0 & 0 & 0 \\ 0 & -1 & 1 & 0 & 0 \\ 0 & 0 & 2A-1 & 1 & 0 \\ 0 & 0 & 0 & -1 & 1 \end{pmatrix} \begin{pmatrix} V_1 \\ V_2 \\ V_3 \\ V_5 \\ V_6 \end{pmatrix} \tag{1}$$

where, $R_H \equiv h/e^2$ is the Hall resistance.

B. Derivation of Andreev reflection probability A

In the current samples, due to the smallness of the Zeeman energy compared to disorder broadening, the QH plateaus at odd filling factors are not well developed. We therefore restrict ourselves to the case of even filling factors, for which we can assume that singlet

s-wave pairing correlations are induced via the proximity effect between co-propagating edge modes with opposite spin-polarization. In first approximation, the effect of Zeeman splitting can be neglected when deriving the expression of A [1]. Without loss of generality, we can set $\nu = 2$. Along the QH-SC interface the QH edge modes for $\nu = 2$ can be described by the effective Bogoliubov-de Gennes Hamiltonian $H_{BdG} = \int dx\ \psi^\dagger(x)\mathcal{H}(x)\psi(x)$ where:

$$\mathcal{H} = v_d(-i\partial_x)\tau_0 - v_d k_F \tau_z + \tilde{\Delta}\tau_x, \tag{2}$$

τ_i are Pauli matrices in particle-hole space, $\psi(x) = \left(c_{x\uparrow},\ c^\dagger_{x\downarrow}\right)^T$, $c^\dagger_{x\sigma}$ ($c_{x\sigma}$) is the creation (annihilation) operator for an electron at position x with spin σ, and $\tilde{\Delta}$ is the superconducting gap induced by proximity in the region of the 2DEG covered by the SC. From the expression of $\mathcal{H}$ we can obtain the transfer matrix which is generally path-dependent. We assume the Hamiltonian is constant along the interface and find,

$$M(L_{sc},\ 0) = e^{i\alpha}\begin{pmatrix} t & r \\ -r^* & t^* \end{pmatrix} \tag{3}$$

relating the outgoing wave function at the end of the QH-SC interface, $x = L_{sc}$, to the incoming wave function at the beginning of the QH-SC interface, $x = 0$ [2]. In Eq. (3) α is a trivial phase and r describes the mixing of electrons and holes along the interface. The Andreev reflection probability is then given by

$$A = |e^{i\alpha}r|^2 = \frac{\sin^2(\delta\phi)}{1 + \left(v_d k_F/\tilde{\Delta}\right)^2} \tag{4}$$

where $\delta\phi$ is the phase difference between the electron-like and hole-like CAES's accumulated along the interface. As stated in the main text, we have $\delta\phi = L_{sc}\delta k$, with $\delta k \equiv |k_F^{(e)} - k_F^{(h)}| = [\tilde{\Delta}^2 + (v_d k_F)^2]^{1/2}/v_d$ the difference between the Fermi wave vectors of the electron-like and hole-like edge modes.

C. Effect of electron tunneling into the superconductor

In the presence of dephasing processes the expression for A given by Eq. (4) should be averaged over $\delta\phi$ to give an average A, $\langle A\rangle$. Given Eq. (4) we have $\langle A\rangle \leq 0.5$, that is smaller than the value $A = 0.55$ extracted from the the experimental measurement. As

mentioned in the main text, one way to reconcile the experimentally measured negative R_D with strong dephasing along the QH-SC interface, is to assume the presence of quasiparticle tunneling into the SC, and the absence of particle-hole symmetry. In this case electron-like quasiparticles can have a larger probability, T, to tunnel into the SC, than hole-like quasiparticles.

For $T \neq 0$, the form of the Landauer-Büttiker equation remains the same, but $2A$ is replaced by $2A + T$. With this modification we can obtain the value of R_D using Eq. (3) in the main text. Figure 10 shows the value of R_D as a function of T and A, consistent with quasiparticle conservation $A + T + R = 1$, where R is the probability of normal reflection at the SC interface. We see that in the limit when $\langle A \rangle$ is maximum, $\langle A \rangle_u = 0.5$, from the experimental value of R_D we extract $T = 0.2$. For the lowest value of $\langle A \rangle$, $\langle A \rangle_l$, consistent with the measured R_D, and quasiparticle conservation, we have $T = 0.8$, corresponding to a strong breaking of particle-hole symmetry.

D. Tight Binding Model

Figure 11 (a) shows schematically the geometry of the system modeled by the tight-binding model. To estimate the properties of the CAES dispersion, for $\nu = 2$, we use the following tight-binding Bogoliubov-de Gennes Hamiltonian:

$$H_{BdG} = \sum_i \psi_i^\dagger \left(4t - \mu\right) \tau_z \psi_i + \sum_{\langle ij \rangle} \psi_i^\dagger \left(-te^{i\phi_{i,j}} \frac{\tau_0 + \tau_z}{2} + te^{-i\phi_{i,j}} \frac{\tau_0 - \tau_z}{2} \right) \psi_j + \sum_i \psi_i^\dagger \left(-\Delta_i \tau_x\right) \psi_i \tag{5}$$

where $\psi_i = \left(c_{i,\uparrow},\ c_{i,\downarrow}^\dagger\right)^T$, $c_{i,\sigma}^\dagger$ $(c_{i,\sigma})$ is the creation (annihilation) operator for an electron at site i with spin σ, τ_i are 2×2 Pauli matrices in particle-hole space, μ_i, Δ_i are the chemical potential and superconducting gap at site i, respectively, and $\phi_{i,j}$ is the Peierls phase introduced to take into account the presence of the magnetic field in the region of the 2DEG not covered by the SC. We assume $\Delta_i = \tilde{\Delta}$ in the region of the 2DEG covered by the SC and $\Delta_i = 0$ in the remainder of the 2DEG. In the region not covered by the SC μ_i is set to a value, μ, that depends on the strength of the magnetic field B, such that $\nu = 2$. We take the hopping parameter $t = 1.323$ eV and lattice spacing $a = 2.0$ nm to model a quadratic dispersion with effective mass $m^* = 0.08 m_e$. We set $\tilde{\Delta} = 1$ meV. Table II shows the fixed parameters used for the tight-binding model. In the region covered by the SC $\mu_i = \mu_s$, and

m^* (m_e)	Δ (meV)	a_{lat} (nm)	$L_y^{(n)}$ (nm)	$L_y^{(sc)}$ (nm)
0.08	1.0	2.0	200.0	600.0

TABLE II. Parameters used in tight binding calculations.

in general $\mu_s \neq \mu$. The magnetic field is in the direction, z, perpendicular to the xy plane to which the 2DEG is confined: $\mathbf{B} = B\hat{z}$. Using the Landau gauge $\mathbf{A} = -By\hat{x}$, and the notation of Fig. 11 (a), the Peierls phase is given by the expression:

$$\phi_{i,j} = -\frac{2\pi B}{\phi_0}\frac{(y_i + y_j)(x_j - x_i)}{2} \tag{6}$$

where (x_i, y_i) are the coordinates of the i^{th} site, $\phi_0 = h/e$ is the quantum Hall magnetic flux quantum.

Figure 11 (b) shows the spectrum obtained using the tight binding model, implemented via the python package Kwant [3]. The in-gap states with large positive velocity describe the QH edge modes at the QH-vacuum interface. The in-gap states with negative velocity, v_d, describe the CAES at the QH-SC interface. Figure 11 (c) shows an example of the profile of the square of the particle-like and hole-like wave functions for the CAES across the QH-SC interface. Finally, Fig. 11 (d) shows the values of $v_d k_F$ for the CAES extracted from results like the ones shown in Fig. 11 (b) for different values of the ratio ℓ_B/ξ_{sc} between the magnetic length ℓ_B and the superconducting coherence length $\xi_{sc} = \frac{2\sqrt{\mu t}}{\pi\Delta}$, and different ratios of μ_s/μ. We see that, in general, as the ratios ℓ_B/ξ_{sc}, μ_s/μ increase, $v_d k_F$ decreases and can be quite smaller than 1.

[1] M. Stone and Y. Lin, Physical Review B - Condensed Matter and Materials Physics 10.1103/PhysRevB.83.224501 (2011).

[2] J. A. M. van Ostaay, A. R. Akhmerov, and C. W. J. Beenakker, Phys. Rev. B **83**, 195441 (2011).

[3] C. W. Groth, M. Wimmer, A. R. Akhmerov, and X. Waintal, New Journal of Physics **16**, 063065 (2014).

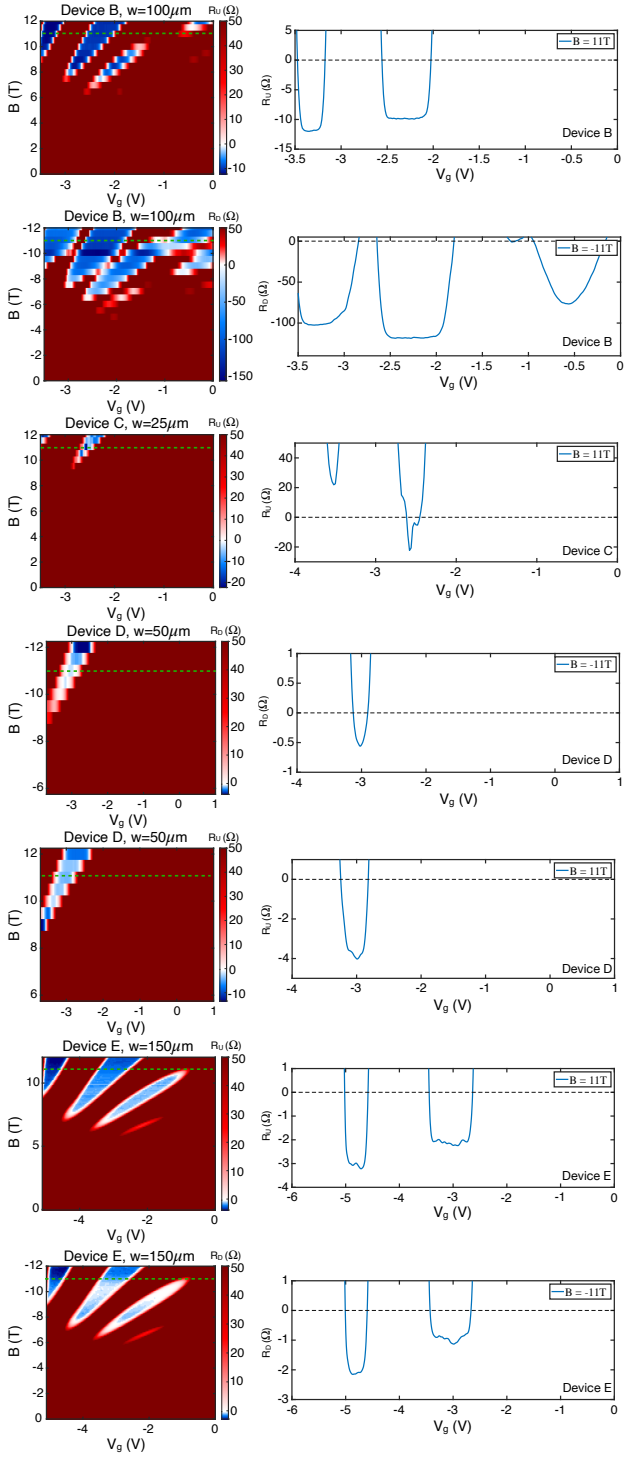

FIG. 8. The downstream resistance of the devices in table. I for different top gate voltages and magnetic field on the left column plus a horizontal cut at $B = \pm 11T$ on the right column. As observed, the negative value in downstream resistance is consistently visible among all these devices though its amplitude varies depending on the fabrication/preparation of each device.

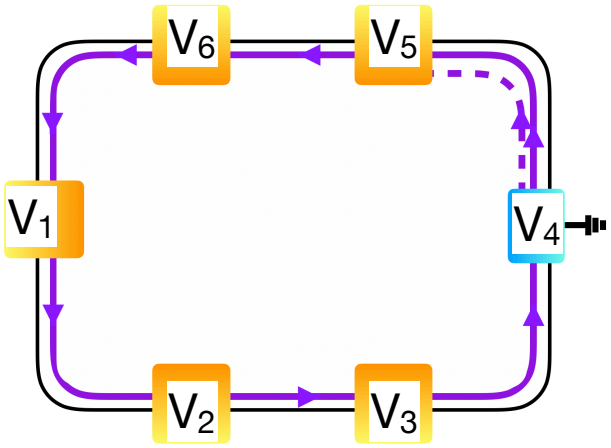

FIG. 9. Six-terminal Hall bar describing edge state transport when one lead is grounded superconductor (blue).

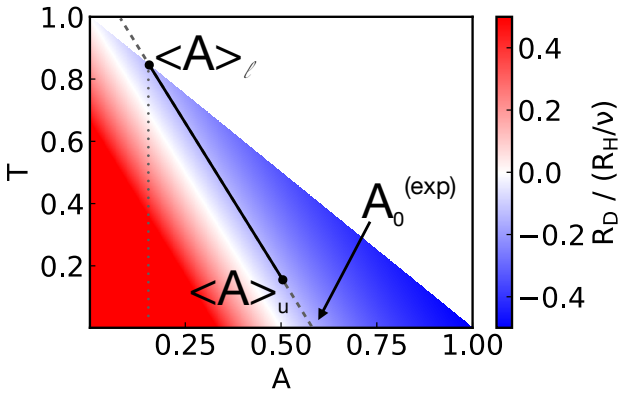

FIG. 10. Colormap of R_D illustrating the upper and lower bounds of $\langle A \rangle$, $\langle A \rangle_u$ and $\langle A \rangle_l$, and corresponding values of T, consistent with measured R_D.

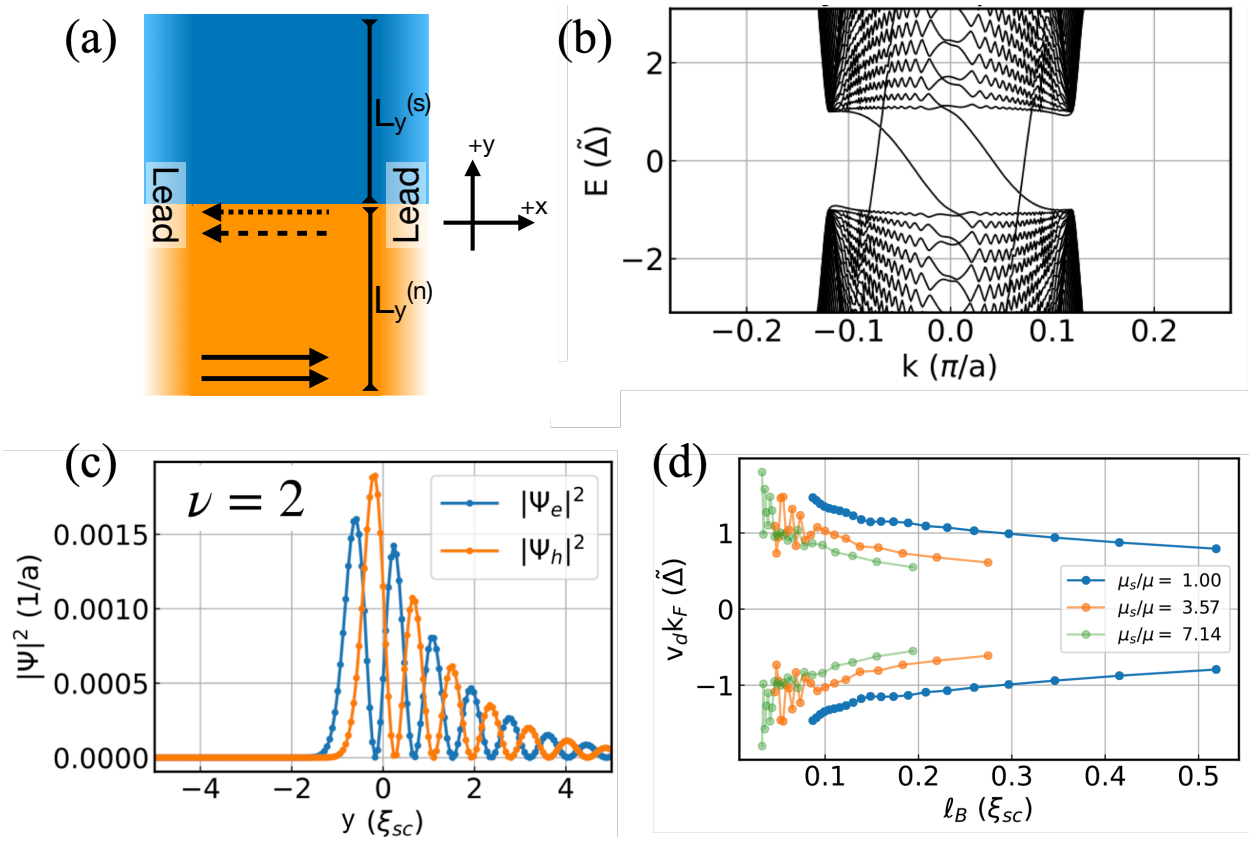

FIG. 11. (a) Geometry of the hybrid NS lead used to calculate the chiral Andreev edge state dispersion. Translational invariance is taken to be in the $+x$-direction. (b) Dispersion showing both trivial edge states (positive velocity) and Andreev edge states (negative velocity) in the spinful LLL for $B = 10$ T. (c) Cut of the electron-like CAES wave function in the lowest Landau level (LLL). The interface between the N and proximitized N regions is at $y = 0$. (d) $v_d k_F$ as a function of magnetic length ℓ_B in units of the superconducting coherence length $\xi_{sc} = \frac{2\sqrt{\mu t}}{\pi\Delta}$ in the proximitized region, for different values of μ_s/μ.